Proceedings of the Combustion Institute 42 (2026) 106430

Contents lists available at ScienceDirect

Proceedings of the Combustion Institute

journal homepage: www.elsevier.com/locate/proci

Probing soot nanoparticle evolution in hydrogen-added counterflow diffusion flames

Maurus Bauer *, Jan A. Dardin, Malte Seitz, Dimosthenis Trimis, Fabian P. Hagen *

Engler-Bunte-Institute, Combustion Technology, Karlsruhe Institute of Technology (KIT), Germany

ARTICLE INFO

Keywords:
Soot formation
Counterflow diffusion flames
Hydrogen addition
Evolution of particle size distribution
Thermal–chemical effect disentanglement

ABSTRACT

Hydrogen (H_2) addition to hydrocarbon flames alters soot yield, morphology, and nanostructure. This study investigates its influence on ethylene (C_2H_4) counterflow diffusion flames by quantifying soot volume fraction, refractive-index function for absorption, and size distributions, while simultaneously characterizing flame structure via OH*, CH*, and Swan band emission as well as temperature profiles. To disentangle the individual effects of H_2 addition, H_2-, He-, and He/Ar-modified flames were compared. The evolution from nascent, weakly light-absorbing nanoparticles of approximately 2–3 nm to mature soot was tracked, and the observed differences were attributed to the disentangled effects. Higher flame temperatures were found to enhance soot formation, whereas H_2-specific chemistry and thermophysical changes associated with H_2 addition acted in a soot-suppressing manner. The amount of added H_2 determines whether the combined effects enhance soot formation at low addition levels or suppress it at higher addition levels, where smaller particles with a less graphitic nanostructure are formed.

Novelty and significance statement: Building on previous studies that separated dilution, thermal, and chemical effects of hydrogen addition on soot formation in hydrocarbon diffusion flames, this work links these effects to the particle-scale evolution of soot. Hydrogen-added ethylene counterflow diffusion flames were designed to disentangle these effects and to quantify, for the first time with hydrogen addition, the evolution of soot particle size distributions from nascent (2–3 nm) to mature primary particles. Using a comprehensive diagnostic toolbox, variations in flame structure, soot volume fraction, size distribution, and optical properties are attributed to isolated effects governing soot formation. The results provide reference data for modeling soot formation and size distributions in a canonical flame configuration. More broadly, the study establishes an experimental framework that can be extended to complex liquid fuels, including conventional and sustainable aviation fuels (SAF), enabling future investigations of hydrogen-assisted combustion strategies for soot and CO_2 mitigation.

1. Introduction

Hydrogen (H_2) addition to hydrocarbon fuels represents a promising pathway toward decarbonization, yet its overall impact on soot formation remains complex and not fully understood. Its effect on soot formation can be attributed to changes in fuel concentration, flame temperature, transport properties, and chemical interactions, with these effects being strongly coupled [1,2]. Extensive investigations in canonical flames — summarized by Wang et al. [3] and Wang and Chung [4] — have explored these effects, with laminar ethylene (C_2H_4) diffusion flames serving as model systems for H_2–soot studies.

To isolate the individual contributions, studies have often compared flames with either H_2 or He added in equal amounts, the latter serving as an inert reference with comparable transport behavior. Using this approach in laminar coflow C_2H_4 diffusion flames, Gülder et al. [2] showed that H_2 suppresses soot formation more strongly than comparable He dilution and attributed the difference between the two cases to an overall chemical suppressive effect of H_2. Subsequent numerical work by Guo et al. [5] supported this interpretation and attributed the chemical suppressive effect of H_2 to reduced H-atom concentrations in soot surface growth regions together with elevated H_2 concentrations in the lower flame region. Gu et al. [6] likewise showed a chemical suppressive effect of H_2 and reported that H_2 is particularly effective in suppressing soot inception. Sun et al. [7] further found that H_2 addition reduces not only soot volume fraction but also the primary particle diameter. Notably, however, N_2 was found in this study to be even more effective than H_2 in suppressing soot formation.

* Corresponding authors.
E-mail addresses: maurus.bauer@kit.edu (M. Bauer), fabian.hagen@kit.edu (F.P. Hagen).

https://doi.org/10.1016/j.proci.2026.106430
Received 16 March 2026; Accepted 9 June 2026
Available online 15 September 2026

Despite these overall suppressive trends, the chemical effect of H_2 in particular remains debated. Steinmetz et al. [8] reported a chemically enhancing effect of H_2 in laminar coflow C_2H_4 diffusion flames. Consistent with this trend, Serrano-Bayona et al. [9] found that, at constant carbon flux, replacing N_2 in the fuel stream with H_2 increased soot volume fraction and led to earlier soot formation. They attributed this enhancement to higher flame temperatures, increased diffusivity, and chemical effects associated with elevated concentrations of soot precursor species.

In C_2H_4 counterflow diffusion flames (CDFs), the role of H_2 has also been examined, but with differing conclusions regarding its effect relative to He. Du et al. [1] investigated the additives N_2, Ar, He, and H_2, and found He to be the most effective in suppressing soot inception. H_2 also exerted a strong suppressive effect, despite increasing flame temperature and thus the flame's propensity for soot formation. They attributed this behavior primarily to preferential diffusion and fuel dilution, while also noting that direct chemical suppression by H_2 may contribute. In contrast, Xu et al. [10] reported that H_2 addition reduces soot volume fraction more strongly than He addition in C_2H_4 CDFs. Their kinetic analysis attributed the inhibiting role of H_2 primarily to suppression of polycyclic aromatic hydrocarbon (PAH) growth and, consequently, soot inception.

While these studies consistently show that dilution reduces soot formation in laminar C_2H_4 diffusion flames, the relative roles of the remaining contributions, particularly the chemical effect, are still not fully resolved. To address this, the present work first investigates the overall effect of increasing H_2 addition on a laminar C_2H_4 CDF by systematically characterizing key chemiluminescent species — OH*, CH*, C_2* — and temperature profiles together with soot metrics, *i.e.*, soot volume fraction, refractive-index function for absorption, and the primary particle size distribution. Two representative H_2-added CDFs are then selected to disentangle the underlying effects. Following the general strategy introduced by Hui et al. [11], the added H_2 is first substituted by He, after which the remaining N_2 is partially replaced by Ar to match the flame temperature of the H_2-added CDF. This approach enables the individual contributions of H_2 addition to soot formation to be disentangled and quantified individually.

2. Design and objective of this study

The CDFs investigated in this work were stabilized in a water-cooled, traversable counterflow (CF) burner consisting of two opposing ducts with an inner diameter of 25 mm and a fixed separation distance of 12.5 mm. Fuel and oxidizer flows were metered by mass flow controllers and passed through 50 μm wire meshes at each duct exit to establish near plug-flow inlet conditions [12]. The streams were supplied through the lower (fuel) and upper (oxidizer) ducts, respectively. Both ducts were surrounded by ring-shaped N_2 sheath flow channels, and exhaust gases were removed through an annular outlet on the fuel side. Further details on the burner design and operating principles are provided elsewhere [13–15].

In this configuration, the base C_2H_4 CDF (see Fig. 1) employed a C_2H_4/N_2 fuel mixture opposed by an N_2/O_2 oxidizer (synthetic air). Hydrogen was added to the fuel stream up to a mole fraction of $x_{H_2} = 0.40$, with the N_2 mole fraction reduced accordingly. For all investigated CDFs, the C_2H_4 flow rate was kept constant at $\dot{V}_{C_2H_4} = 1.440\ \mathrm{L\,min^{-1}}$ and the C_2H_4 mole fraction was fixed at $x_{C_2H_4} = 0.31$, ensuring a constant carbon flux; consequently, the dilution effect associated with carbon replacement is eliminated. This also results in a constant fuel-side duct exit velocity, consistent with the approach used by Xu et al. [10] in their study of H_2-added C_2H_4 CDFs. In addition, the fuel and oxidizer streams were adjusted to satisfy the momentum balance $\rho_{\mathrm{Fuel}}\, u^2_{\mathrm{Fuel}} = \rho_{\mathrm{Ox.}}\, u^2_{\mathrm{Ox.}}$, where ρ_i and u_i denote the density and axial velocity of the respective streams. This condition is commonly imposed in CDF studies to ensure that the stagnation plane is located midway between the two opposing ducts [12]. Further details on the operating conditions, including flow rates, duct exit velocities, and the strain rate a_2 defined according to Seshadri and Williams [16], are provided in the Supplementary Material.

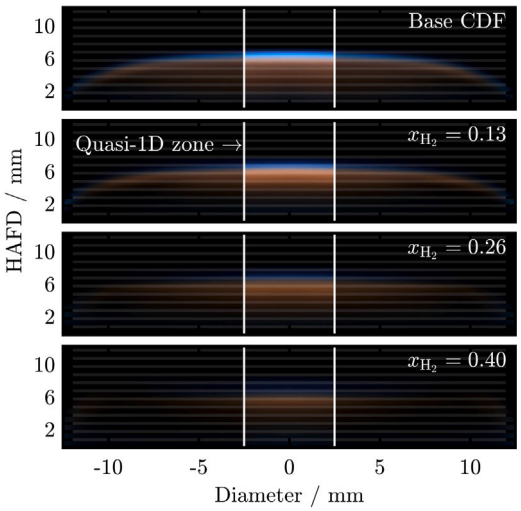

Fig. 1. Flame images of the base C_2H_4 CDF and the corresponding H_2-added cases with increasing x_{H_2}.

To disentangle the different effects of H_2 addition to the base flame, two representative CDFs at $x_{H_2} = 0.13$ and 0.26 (see Fig. 1) were examined in more detail. For each selected case, the added H_2 was first replaced by He. In a second step, the remaining N_2 was replaced by Ar to recover the adiabatic flame temperature of the H_2-added case, involving complete replacement on the fuel side and partial replacement on the oxidizer side. This temperature adjustment is achieved by modifying the mixture heat capacity, as commonly applied in previous studies [1,17]. For disentangling the individual effects, each selected H_2-added case was therefore represented by three complementary configurations:

(A) H_2-added CDF:
$C_2H_4/H_2/N_2 \longleftrightarrow N_2/O_2$
This configuration represents the overall effect of H_2 addition relative to the base flame while excluding the dilution effect associated with carbon replacement.

(B) He-substituted CDF:
$C_2H_4/He/N_2 \longleftrightarrow N_2/O_2$
This configuration removes the chemical effect of H_2 by replacing it with He, which serves as an inert reference with comparable transport behavior.

(C) He/Ar-substituted CDF:
$C_2H_4/He/Ar \longleftrightarrow N_2/Ar/O_2$
This configuration reproduces the adiabatic flame temperature of case (A) without H_2, thereby enabling the chemical effect of H_2 to be isolated under matched thermal conditions.

For all investigated CDFs, the flame structure was characterized using axial profiles of OH*, CH*, and C_2* measured by emission spectroscopy, together with temperature profiles obtained by thermocouple thermometry. Two-color time-resolved laser-induced incandescence (2C-TiRe-LII) was used to analyze soot formation in terms of soot volume fraction f_v, refractive-index function for absorption $E(m, \lambda_{\mathrm{NIR}})$ and the primary particle size distribution $P(d_p)$. In addition, the mobility size distributions $P(d_m)$ of evolving soot particles were determined using the aerosol probe introduced by Hagen et al. [13] and numerically supported by Kalbhor et al. [18], coupled with a differential mobility sizer.

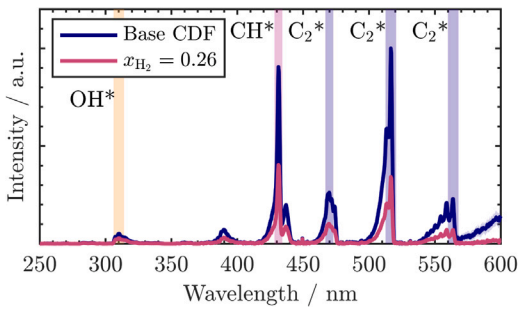

Fig. 2. Baseline-corrected emission spectra recorded at HAFD = 6.5 mm for the base CDF and the H_2-added flame. The spectra are corrected for the wavelength-dependent response of the optical setup. Colored bands indicate the integration windows used for the chemiluminescence analysis of the OH*, CH*, and C_2* emissions.

3. Diagnostics

In this section, the diagnostics used to characterize the CDF structure and soot particle formation and evolution are outlined.

3.1. Flame structure characterization

Broadband flame emission imaging enabled visualization of the overall flame structure and of the reaction and soot formation zones (see Fig. 1).

Complementary, spatially resolved emission spectra in the wavelength range of 250–600 nm were recorded to capture OH*, CH*, and C_2* Swan band emissions as a function of height above the fuel duct (HAFD). Radiation emitted from the flame was collected at different HAFDs using an imaging lens defining the observation volume. The intermediate image was spatially filtered by a pinhole in the image plane to restrict the measurement region. The transmitted radiation was subsequently collimated and focused into an optical fiber that guided the signal to a Czerny–Turner spectrograph equipped with a CCD detector. The effective probe volume, defined by the imaging optics and pinhole, resulted in a spatial resolution below 400 µm. Spectral intensities were corrected for the wavelength-dependent response of the optical system using a calibrated tungsten emission source.

Resulting baseline-corrected spectra at a HAFD of 6.5 mm for the base CDF and the H_2-substituted CDF with $x_{H_2} = 0.26$ are shown in Fig. 2. The OH* chemiluminescence corresponds to the $A^2\Sigma^+ \rightarrow X^2\Pi$ transition, while CH* emission arises from the $A^2\Delta \rightarrow X^2\Pi$ transition. The spectra also include the $\Delta v = 0$ Swan band near 516 nm and adjacent $\Delta v = \pm 1$ and ± 2 transitions of the $d^3\Pi_g$–$a^3\Pi_u$ electronic system [19].

Axial temperature profiles were measured with an S-type thermocouple probe as described in [13–15,20]. The 100 µm thermowires were tensioned parallel to the reaction zone by a spring mechanism and coated with ZrO_2 to suppress catalytic effects. Measured temperatures were corrected for radiation losses according to Shaddix [21]. Considering the standard deviation of repeated measurements and the uncertainty associated with the radiation correction, the overall uncertainty of the reported temperatures is estimated to be ±80 K; see, *e.g.*, [15].

3.2. Soot diagnostics

2C-TiRe-LII, as described in previous work [13,15], was used to determine the soot volume fraction f_v, the refractive-index function for absorption $E(m, \lambda_{NIR})$, and the primary particle size distribution $P(d_p)$.

Upon absorption of a nanosecond laser pulse, soot particles undergo a rapid temperature rise followed by cooling dominated by heat conduction to the surrounding gas in the low-fluence regime [22,23]. At the near-infrared excitation wavelength $\lambda_{NIR} = 1064$ nm, the absorption function $E(m, \lambda_{NIR})$ is sensitive to the nanostructure and/or maturity of the soot particles [24–26]. Increasing nanostructural ordering and larger basic structural units (BSUs) enhance the absorption of low-energy photons, resulting in higher values of $E(m, \lambda_{NIR})$ [25,26].

According to [27], $E(m, \lambda_{NIR})$ was determined from the measured particle temperatures before and after laser pulse absorption under low-fluence conditions. In this regime, the temperature increase induced by laser heating can be approximated by

$$E(m, \lambda_{NIR}) \approx \frac{\lambda_{NIR}\, \rho_p c_p}{6\pi f_{exc}} \left(T_p^* - T_p^0 \right), \tag{1}$$

where T_p^0 and T_p^* denote the particle temperatures before and immediately after laser pulse absorption, respectively, f_{exc} is the laser fluence integrated over the pulse duration, ρ_p is the particle density, and c_p is the mass specific heat capacity of the particles [25,27,28]. The initial particle temperature T_p^0 was assumed to be equal to the local gas temperature. The uncertainty of $E(m, \lambda_{NIR})$ arises mainly from uncertainties in particle temperature, particle density, and heat capacity. Following the analysis reported in [15], the resulting uncertainty is estimated to be about 20% for mature soot particles and up to about 40% for nascent soot particles.

In the low-fluence regime, the TiRe-LII signal decay is governed by conductive heat transfer between the heated particles and the surrounding gas [22,23]. In this regime, particle sublimation is negligible. Since the conductive cooling rate scales with particle surface area, smaller particles cool faster than larger ones. Consequently, the temporal decay of the TiRe-LII signal contains information on $P(d_p)$. The distribution was assumed to follow a log-normal function characterized by its count median diameter (CMD) and geometric standard deviation σ_g. The CMD of $P(d_p)$ was obtained by fitting numerically simulated signal decays to the measured TiRe-LII signals using the Karlsruhe model [29,30]. In accordance with [15], a variable σ_g was applied as a function of HAFD. As detailed in that study, the uncertainty of the CMD of $P(d_p)$ derived from the TiRe-LII decays is mainly governed by the assumed σ_g, uncertainties in the local gas temperature, and the extrapolation of optical properties. The CMD of $P(d_p)$ is therefore conservatively reported with an expanded uncertainty below 20%.

The soot volume fraction f_v was derived from the same low-fluence measurements using the auto-compensating approach introduced in [31] and adopted in [15]. In this approach, f_v is determined from the particle temperature directly after laser pulse absorption without calibration against a reference flame. The resulting f_v values were compared in [15] with values obtained from the classical plateau-fluence approach using a reference flame calibration. For soot volume fractions up to 500 ppb, both methods agreed within ±15%, while deviations below 30% were observed for higher f_v values, consistent with the overall measurement uncertainties.

The laser-optical setup, described in detail elsewhere [15], employed a Q-switched Nd:YAG laser operating at 10 Hz. The laser fluence was controlled using a rotating half-wave plate and a polarizing beam splitter, and it was monitored by a calibrated photodiode. The laser beam was relay-imaged into the detection volume with a magnification of 1:1. The 2C-TiRe-LII signals were detected at 120° relative to the laser axis using two photomultipliers equipped with interference filters centered at 450 nm and 650 nm, respectively. The signal recording was carried out with a digital oscilloscope.

Complementary to 2C-TiRe-LII, which provides $P(d_p)$, differential mobility sizing was applied to determine the mobility size distribution $P(d_m)$. This approach allows characterization of nascent and weakly NIR-absorbing particles and reveals possible bimodal features of the evolving particle ensemble, thereby extending the accessible size range beyond optical diagnostics.

Particle-laden flame gas was extracted from the CDFs using an aerosol probe developed and characterized in detail in [13], enabling

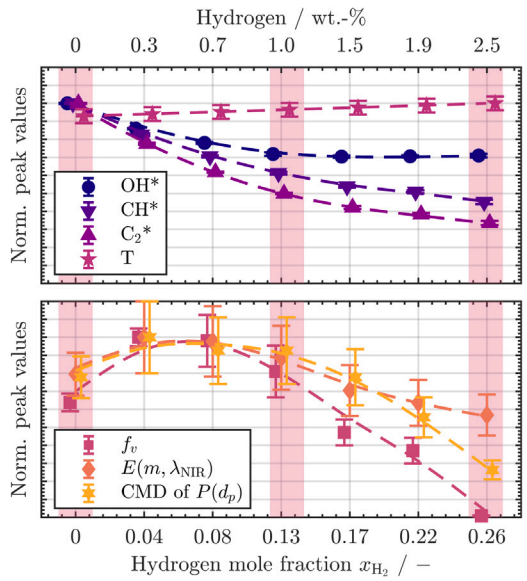

Fig. 3. Normalized peak values characterizing the flame structure (top) and soot-related metrics (bottom) as a function of H_2 addition to the base C_2H_4 CDF. All quantities are normalized by their respective peak values in the base flame, *i.e.*, T_{max} = 1861 K, f_v = 571 ppb, $E(m, \lambda_{NIR})$ = 0.35, and CMD of $P(d_p)$ = 21 nm. The highlighted regions indicate the flames selected for detailed analysis.

spatially resolved sampling. Rapid N_2 quenching of the sampled aerosol freezes soot particle surface growth, coagulation, and oxidation, which is essential to preserve the particle size distribution during sampling [32]. The probe features a concentric double-wall quartz geometry with a conical tip and annular dilution gas inlet, designed to minimize flame disturbance while ensuring efficient mixing and rapid quenching of the extracted flame gas. The sampling rate is controlled via the pressure drop Δp_0 across the probe orifice and the dilution gas flows, which together define the dilution ratio (DR). The DR was determined using the CO_2 tracer method proposed by Camacho et al. [33], yielding an empirical correlation between Δp_0 and DR up to values of about 2×10^3. This correlation was used to convert measured number concentrations into absolute $P(d_m)$. Particle losses in the probe, transfer lines, and instruments were corrected according to [13]. The uncertainty of the derived $P(d_m)$, and thus of CMD and f_v, arises mainly from uncertainties in the determination of DR, particle losses in the probe and transfer lines, and the fact that sampling occurs from a finite probe volume rather than a point location. To account for these contributions, both quantities are conservatively reported with an overall uncertainty of 30%. However, comparison with non-intrusive 2C-TiRe-LII measurements confirmed negligible perturbation of the CDF structure and consistent particle number densities [13].

The diluted aerosol was classified by electrical mobility using a differential mobility analyzer (DMA) and detected by a condensation particle counter (CPC) to obtain $P(d_m)$. Prior to classification, the aerosol passed through a soft X-ray neutralizer to establish a well-defined charge equilibrium.

4. Results and discussion

Fig. 3 illustrates the response of the base CDF to H_2 addition up to x_{H_2} = 0.26, in terms of normalized peak values of flame structure markers and soot-related metrics obtained by 2C-TiRe-LII.

The soot metrics f_v, $E(m, \lambda_{NIR})$, and the CMD of $P(d_p)$ initially increase up to x_{H_2} = 0.04, remain nearly unchanged at the next addition level (x_{H_2} = 0.08), and then decrease markedly with further H_2 addition. At low H_2 fractions, this behavior may be related to changes in the radical pool, including an increased availability of highly reactive H radicals, which can promote hydrocarbon radical formation, facilitate PAH growth via pathways such as HACA, and thereby enhance the formation of early soot precursors. A similar initial increase has also been reported for H_2-added C_2H_4 diffusion flames at constant carbon flux and has been attributed to increased diffusivity, elevated flame temperatures, and higher concentrations of soot precursors associated with small H_2 additions [8,9]. Finally, the observed initial increase may partly reflect the slight decrease in the strain rate, relative to the base flame across the H_2-addition series. This variation arises from the chosen experimental design: maintaining a constant carbon flux while satisfying the momentum balance between the fuel and oxidizer streams leads to small changes in the oxidizer-side duct exit velocity and therefore in the strain rate, as described in detail in the Supplementary Material. Xu et al. [10] likewise reported strain rate variations associated with H_2 addition and found their influence on soot formation to be negligible. Accordingly, while the initial rise in the soot metrics may include a contribution from the accompanying variation in strain rate, the observed trend is also consistent with previously reported effects of small H_2 additions on soot precursor formation.

At higher H_2 addition levels, Fig. 3 indicates that H_2 exerts a strong soot suppressing effect, as reflected by the reduced f_v and CMD of $P(d_p)$, in agreement with previous findings reported by Xu et al. [10]. Moreover, the decrease in $E(m, \lambda_{NIR})$ indicates smaller and less ordered BSUs, *i.e.*, less mature soot particles with reduced NIR absorption, which is consistent with the findings of Choi et al. [34], who reported that H_2 addition reduces the degree of graphitization of soot particles.

By comparison, the flame structure markers — OH*, CH*, C_2*, and T — exhibit largely monotonic trends with increasing H_2 addition. Across the range considered in Fig. 3, the peak temperature increases linearly, whereas the normalized peak intensities of CH* and C_2* decrease. OH* decreases up to about x_{H_2} = 0.17 and then remains approximately constant, consistent with numerical simulations performed in this work using the GRI-Mech 3.0 [35], extended by the chemiluminescence reaction set proposed by Kathrotia et al. [36]. A rate-of-production analysis provided in the Supplementary Material reveals a compensation between dominant OH* formation and consumption pathways.

As will be shown below, the soot volume fraction decreases when moving from the H_2-added CDFs to the corresponding He-substituted flames used to disentangle the effects on soot formation. Since the He-substituted flame for the H_2-added case with x_{H_2} = 0.26 is the highest H_2 addition level at which the soot metrics can still be determined, this case was selected to probe conditions close to the sooting limit. This regime marks the transition between soot-forming and non-sooting conditions and thus provides insight into the onset of particle formation. Under these conditions, however, the uncertainty of the 2C-TiRe-LII signal analysis increases substantially. While $E(m, \lambda_{NIR})$ can still be determined by increasing the laser fluence, the quantification of $P(d_p)$ and f_v becomes increasingly uncertain. To further characterize particle formation under these near-sooting-limit boundary conditions, mobility size distributions $P(d_m)$ were therefore measured as a function of HAFD using aerosol sampling and differential mobility sizing, as described in Section 3.2. The resulting distributions are shown in Fig. 4.

All investigated flames were soot formation (SF) flames with a stoichiometric mixture fraction of $Z_{st} < 0.5$, such that soot formed between the flame front and the stagnation plane (SP) is convected toward the latter without oxidation [4,37]. Consequently, the observed evolution of $P(d_m)$ reflects only soot formation processes, *i.e.*, particle inception, surface growth, and coagulation, the latter comprising coalescence and aggregation. The distributions reveal soot particle inception on both the fuel and oxidizer sides of the SP located at HAFD = 5.5 mm. As shown in Fig. 4, nascent particles with diameters of about 2–3 nm are detected most clearly on the fuel side of the SP at HAFD = 4.5 mm and 5.0 mm. In this region, $P(d_m)$ broadens, its maximum shifts to larger d_m, and the number of the smallest particles declines, indicating progressive

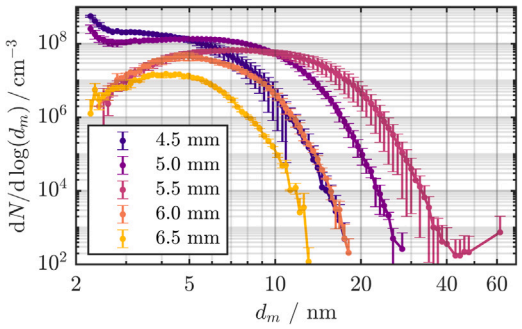

Fig. 4. $P(d_m)$ for different HAFDs measured by aerosol sampling and mobility sizing in the H_2-added CDF with $x_{H_2} = 0.26$.

conversion of nascent particles into larger ones by surface growth and coagulation during convection toward the SP.

These trends may also indicate a transition from inception-dominated to growth-dominated conditions and thus suggest a spatial decoupling of nascent particle formation and subsequent particle growth. On the oxidizer side of the SP, the rightward broadening of $P(d_m)$ and the shift of its maximum likewise indicate progressive particle growth; however, the nearly unchanged number of the smallest particles suggests that nascent particle formation persists in parallel. At the SP itself (HAFD = 5.5 mm), $P(d_m)$ exhibits a weak secondary contribution at mobility diameters larger than 40 nm, suggesting the onset of aggregate formation near the SP.

To further interpret the overall impact of H_2 addition to the C_2H_4 base CDF, the case at $x_{H_2} = 0.26$ is analyzed to disentangle the underlying effects, as described in Section 2. Fig. 5 shows flame images of the four CDFs considered. A first qualitative comparison already suggests that, when added in equal amounts to the base CDF, He suppresses soot formation more strongly than H_2, as reflected by the weaker soot luminosity of the He-substituted flame. At the same time, the He/Ar-substituted CDF exhibits the strongest soot luminosity among the four flames, indicating the highest soot loading. To disentangle and quantify the contributions underlying this behavior, the four CDFs are considered along the sequential modification path: base CDF → He-substituted CDF → He/Ar-substituted CDF → H_2-added CDF. Within this sequential modification path, the transition from the base to the He-substituted CDF captures the thermophysical modification associated with replacing N_2 by He, which serves as an inert reference gas with transport properties similar to those of H_2. The transition from the He- to the He/Ar-substituted CDF isolates the thermal effect, and the comparison between the thermally matched He/Ar-substituted and H_2-added CDFs isolates the chemical effect of H_2 addition. As described in Section 2, the C_2H_4 flow rate was kept constant and the C_2H_4 mole fraction was fixed at $x_{C_2H_4} = 0.31$ for all cases, thereby eliminating the dilution effect associated with carbon replacement. Since the carbon flux is kept constant, the transition from the base CDF to the He-substituted CDF is accompanied by a slight change in strain rate, reported as negligible by Xu et al. [10], and therefore does not represent a purely thermophysical modification. By contrast, the strain rate is consistent across the H_2-added, He-substituted, and He/Ar-substituted CDFs, *i.e.*, $a_2 = 47 \pm 1\ s^{-1}$.

The corresponding axial temperature profiles measured for these flames and those predicted numerically using the POLIMI mechanism [38] are compared in Fig. 6 and provide the thermal basis for disentangling the effects.

The experimental data and numerical predictions show qualitatively similar trends, although the calculations do not fully reproduce the absolute peak temperatures. Specifically, the peak temperatures of the base and He-substituted CDFs are overpredicted, whereas those of the H_2-added and He/Ar-substituted CDFs are underpredicted.

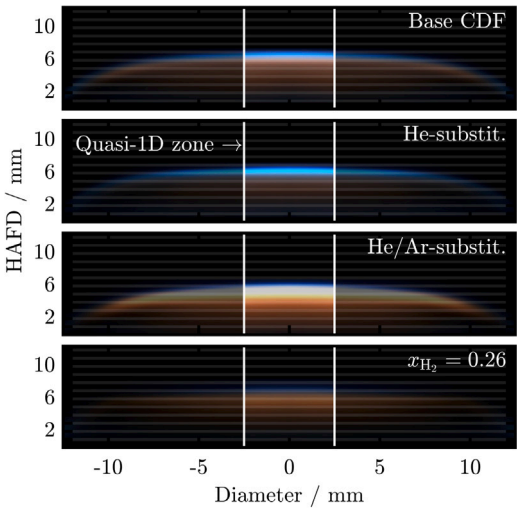

Fig. 5. Flame images of the four CDFs considered to disentangle the effects at $x_{H_2} = 0.26$: the base CDF, the H_2-added CDF (A), the He-substituted CDF (B), and the He/Ar-substituted CDF (C).

Both experiment and simulation nevertheless show that the H_2-added flame exhibits the highest peak temperature, T_{max}, and that the He/Ar-substituted case reproduces it well (see Fig. 6). In the measurements, the difference in T_{max} between these two flames is only 9 K, indicating closely matched thermal conditions and thus allowing the chemical effect of H_2 addition to be isolated. Both experimental data and simulations also show a small temperature difference between the base and He-substituted CDFs, with the latter exhibiting a lower T_{max} by about 28 K.

Fig. 6 also shows the peak regions of the measured chemiluminescence signals. For the base CDF as well as the He- and He/Ar-substituted cases, the regions of peak OH*, CH*, and C_2* emission overlap closely, indicating a narrow reaction zone. In contrast, only the H_2-added CDF exhibits a broadened OH* zone together with a shift of the Swan band emission peak toward the fuel side, suggesting partial C_2H_4/H_2 stratification, which may result from preferential diffusion.

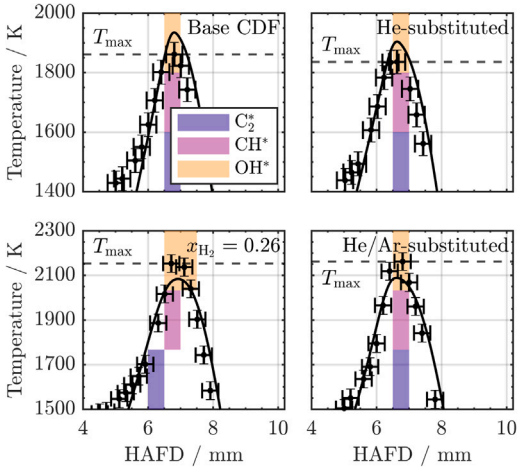

Fig. 6. Temperature profiles and peak emission regions of OH*, CH*, and C_2* for the base CDF and cases (A), (B), and (C) at $x_{H_2} = 0.26$. Symbols represent experimental data, while solid lines correspond to simulations using the POLIMI mechanism [38]. Colored bands mark the axial regions of peak emission of the chemiluminescent species.

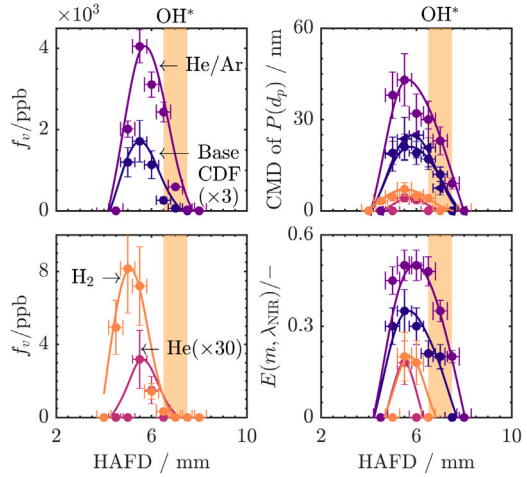

Fig. 7. Soot metrics, f_v, $E(m, \lambda_{NIR})$, and the CMD of $P(d_p)$, as a function of HAFD for the base CDF and cases (A), (B), and (C) at $x_{H_2} = 0.26$. For the two CDFs close to the sooting limit, *i.e.*, the He-substituted and the H_2-added CDFs, f_v and the CMD of $P(d_p)$ are inferred from mobility sizing, whereas for the He/Ar-substituted and the base CDF, 2C-TiRe-LII is employed. For the base CDF, the CMD from aerosol sampling and mobility sizing is additionally shown as a second blue curve with triangle markers. Both methods yield CMD values that agree within the discussed uncertainty, providing consistent and complementary estimates.

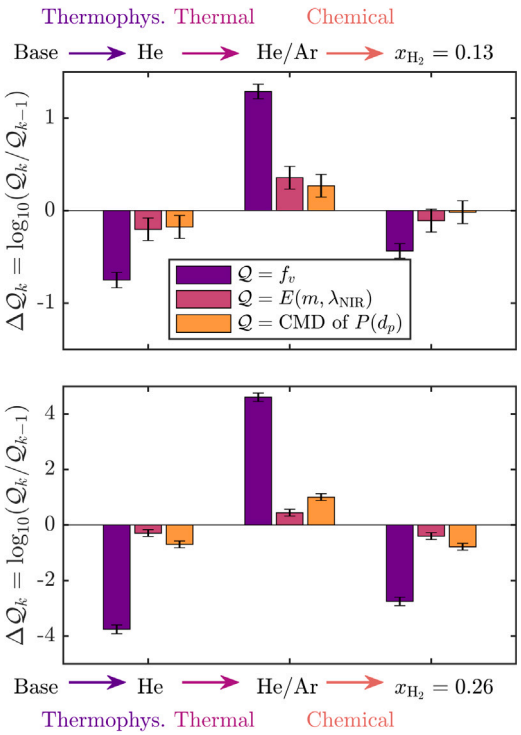

Fig. 8. Logarithmic changes of soot metrics at HAFD = 5.5 mm along the sequential modification path base CDF → He-substituted CDF → He/Ar-substituted CDF → H_2-added CDF for $x_{H_2} = 0.13$ and 0.26, representing the isolated thermophysical, thermal, and chemical effects, respectively.

Fig. 7 compares the corresponding soot metrics f_v, $E(m, \lambda_{NIR})$, and the CMD of $P(d_p)$ for the four CDFs considered to disentangle the underlying effects on soot formation at $x_{H_2} = 0.26$. Taking into account the thermal matching between the H_2-added and He/Ar-substituted cases established by Fig. 6, the changes in these soot metrics can now be interpreted in terms of the thermophysical, thermal, and chemical effect along the sequential modification path. At HAFD = 5.5 mm, corresponding to the SP and thus to the peak soot metrics, the thermophysical step from the base to the He-substituted CDF strongly suppresses soot formation (see Fig. 7). All soot metrics decrease sharply: f_v drops from 571 ppb to 0.10 ppb, the CMD of $P(d_p)$ from 21.0 nm to 4.2 nm, and $E(m, \lambda_{NIR})$ from 0.35 to 0.18. Although the absolute f_v approaches the detection limit of mobility sizing, a monomodal distribution of nascent particles with d_m = 2–4 nm is still inferred, corresponding to $f_v < 1$ ppb. Under these near-sooting-limit conditions, $E(m, \lambda_{NIR})$ can still be determined by 2C-TiRe-LII using increased laser fluence, albeit with higher uncertainty. The strong suppression is consistent with the corresponding flame image (see Fig. 5). The subsequent thermal step, *i.e.*, the transition from the He- to the He/Ar-substituted CDF, reverses this suppression. As T_{max} increases (see Fig. 6), f_v, the CMD of $P(d_p)$, and $E(m, \lambda_{NIR})$ all increase markedly, reaching 4050 ppb, 43.0 nm, and 0.50, respectively. Finally, comparison of the thermally matched He/Ar-substituted and H_2-added CDFs isolates the chemical effect of H_2 addition. All three soot metrics decrease again (see Fig. 7), confirming that the chemical effect of H_2 is suppressive under the present conditions.

The CMD values obtained by the two methods agree within the discussed uncertainty, indicating that both diagnostics provide complementary and mutually consistent estimates of the CMD.

While the stepwise changes along the sequential modification path can be discussed directly in terms of the absolute values of the soot metrics, Fig. 8 provides a more compact representation of this effect disentangling at HAFD = 5.5 mm for both $x_{H_2} = 0.26$ and $x_{H_2} = 0.13$. For a general quantity $\mathcal{Q} \in \{f_v,\ E(m, \lambda_{NIR}),\ \text{CMD of } P(d_p)\}$, each bar denotes the logarithmic change along the modification path from state $k-1$ to state k, expressed in decades. This representation is particularly suitable for the present system, as the investigated quantities vary over multiple orders of magnitude. It also yields an additive decomposition, in which the individual thermophysical, thermal, and chemical effects sum exactly to the total logarithmic change between the base and the H_2-added CDF.

The normalized peak values of the soot metrics — f_v, $E(m, \lambda_{NIR})$, and the CMD of $P(d_p)$ — in Fig. 3 show only slight changes between the base and the H_2-added CDF at $x_{H_2} = 0.13$. This is reflected in the overall logarithmic changes from the base to the H_2-added flame, which amount to +0.10 for f_v, +0.08 for the CMD of $P(d_p)$, and +0.05 for $E(m, \lambda_{NIR})$. Fig. 8, however, shows that this weak net response results from pronounced individual contributions. Specifically, the thermophysical and chemical effects are clearly soot-suppressing, whereas the thermal effect promotes soot formation.

For the $x_{H_2} = 0.26$ case, the same qualitative pattern is retained but the effects are more pronounced. The combined thermophysical and chemical contributions outweigh the opposing thermal effect, leading to a net reduction in all soot metrics and thus to a lower soot volume fraction and smaller, less mature primary particles relative to the base CDF.

The thermal effect, which is the strongest individual contribution in both the $x_{H_2} = 0.13$ and $x_{H_2} = 0.26$ cases, can be readily interpreted from the temperature profiles shown in Fig. 6: between the He- and He/Ar-substituted CDFs, T_{max} increases by about 325 K, and all three soot metrics increase accordingly. The chemically suppressive role of H_2 identified here may be explained by the kinetic analysis of Xu et al. [10], who attributed soot reduction in C_2H_4 CDFs mainly to suppressed PAH growth and, consequently, soot inception. Their study, however, found H_2 to suppress soot formation more strongly than He, whereas in the present work the strongest overall soot suppression is observed for the He-substituted CDF. This pronounced thermophysical effect cannot be explained by temperature changes alone, since the difference in T_{max} between the base and He-substituted CDFs remains below 30 K (see Fig. 6), whereas the reduction in soot formation is

substantial. Du et al. [1] likewise found He to be more effective than H_2 in suppressing soot inception in C_2H_4 CDFs and related this behavior primarily to preferential diffusion and fuel dilution, while Axelbaum et al. [39] showed that soot suppression in C_2H_4 CDFs becomes stronger with increasing additive diffusivity. The pronounced thermophysical effect observed in the present study points in the same direction and suggests that preferential diffusion may play an important role in the soot-suppressive effect of H_2 addition.

5. Concluding remarks

The impact of H_2 addition on soot formation in a C_2H_4 CDF was investigated by disentangling the individual effects. The main conclusions are as follows:

1. When fuel dilution is suppressed, the impact of H_2 addition on soot formation is governed by a competition between thermophysical, thermal, and chemical effects, with the thermophysical and chemical effects suppressing soot formation and the thermal effect promoting it as the strongest individual contribution.
2. The H_2 addition level appears to determine whether the combined effects enhance or suppress soot formation, with low H_2 addition levels leading to either a slight enhancement of soot formation or a near compensation of the individual effects.
3. At higher H_2 addition levels, the combined suppressive thermophysical and chemical effects dominate over the thermal enhancement, leading to lower f_v as well as smaller and less mature soot particles, as reflected by lower CMD of $P(d_p)$ and $E(m, \lambda_{NIR})$ values.

CRediT authorship contribution statement

Maurus Bauer: Writing – original draft, Investigation, Formal analysis, Conceptualization. **Jan A. Dardin:** Writing – review & editing, Investigation, Formal analysis. **Malte Seitz:** Writing – review & editing, Investigation, Formal analysis. **Dimosthenis Trimis:** Writing – review & editing, Resources. **Fabian P. Hagen:** Writing – original draft, Visualization, Supervision, Investigation, Formal analysis, Conceptualization.

Declaration of competing interest

The authors declare that they have no known competing financial interests or personal relationships that could have appeared to influence the work reported in this paper.

Acknowledgments

The authors would like to thank the German Federal Ministry for Economic Affairs and Energy (BMWE) for the financial support (grant number: 03EE5137C).

Appendix A. Supplementary data

Supplementary material related to this article can be found online at https://doi.org/10.1016/j.proci.2026.106430.

References

[1] D.X. Du, R.L. Axelbaum, C.K. Law, Soot formation in strained diffusion flames with gaseous additives, Combust. Flame 102 (1–2) (1995) 11–20.
[2] Ö.L. Gülder, D. Snelling, R. Sawchuk, Influence of hydrogen addition to fuel on temperature field and soot formation in diffusion flames, Proc. Combust. Inst. 26 (2) (1996) 2351–2358.
[3] Y. Wang, M. Gu, Y. Zhu, L. Cao, B. Zhu, J. Wu, Y. Lin, X. Huang, A review of the effects of hydrogen, carbon dioxide, and water vapor addition on soot formation in hydrocarbon flames, Int. J. Hydrog. Energy 46 (61) (2021) 31400–31427.
[4] Y. Wang, S.H. Chung, Soot formation in laminar counterflow flames, Prog. Energy Combust. Sci. 74 (2019) 152–238.
[5] H. Guo, F. Liu, G.J. Smallwood, Ö.L. Gülder, Numerical study on the influence of hydrogen addition on soot formation in a laminar ethylene-air diffusion flame, Combust. Flame 145 (1–2) (2006) 324–338.
[6] M. Gu, H. Chu, F. Liu, Effects of simultaneous hydrogen enrichment and carbon dioxide dilution of fuel on soot formation in an axisymmetric coflow laminar ethylene/air diffusion flame, Combust. Flame 166 (2016) 216–228.
[7] Z. Sun, B. Dally, G. Nathan, Z. Alwahabi, Effects of hydrogen and nitrogen on soot volume fraction, primary particle diameter and temperature in laminar ethylene/air diffusion flames, Combust. Flame 175 (2017) 270–282.
[8] S.A. Steinmetz, H.A. Ahmed, W.R. Boyette, M.J. Dunn, W.L. Roberts, A.R. Masri, Effects of ammonia and hydrogen on the sooting characteristics of laminar coflow flames of ethylene and methane, Fuel 307 (2022) 121914.
[9] R. Serrano-Bayona, F. Campuzano, F. Aydin, T. Mitra, P. Liu, W.L. Roberts, Effects of hydrogen and ammonia substitution on morphological and optical parameters of soot aggregates in ethylene/air laminar coflow diffusion flames, Exp. Therm. Fluid Sci. 174 (2026) 111698.
[10] L. Xu, F. Yan, Y. Wang, S.H. Chung, Chemical effects of hydrogen addition on soot formation in counterflow diffusion flames: Dependence on fuel type and oxidizer composition, Combust. Flame 213 (2020) 14–25.
[11] X. Hui, D. Zheng, W. Tan, X. Xue, W. Liu, The effects of hydrogen addition on soot formation in counterflow diffusion n-heptane flames, Int. J. Hydrog. Energy 48 (23) (2023) 8707–8715.
[12] U. Niemann, K. Seshadri, F.A. Williams, Accuracies of laminar counterflow flame experiments, Combust. Flame 162 (4) (2015) 1540–1549.
[13] F.P. Hagen, P. Vlavakis, M. Seitz, T. Klövekorn, H. Bockhorn, R. Suntz, D. Trimis, Soot nanoparticle sizing in counterflow flames using in-situ particle sampling and differential mobility analysis verified with two-colour time-resolved laser-induced incandescence, Proc. Combust. Inst. 39 (1) (2023) 1119–1128.
[14] F.P. Hagen, P. Vlavakis, H. Bockhorn, R. Suntz, D. Trimis, From molecular to sub-μ m scale: The interplay of precursor concentrations, primary particle size, and carbon nanostructure during soot formation in counter-flow diffusion flames, Combust. Flame 258 (2023) 112729.
[15] P. Vlavakis, F.P. Hagen, A. Loukou, D. Trimis, Soot formation in iso-octane counterflow diffusion flames, Combust. Flame 282 (2025) 114513.
[16] K. Seshadri, F.A. Williams, Laminar flow between parallel plates with injection of a reactant at high Reynolds number, Int. J. Heat Mass Transfer 21 (1978) 251–253.
[17] R.L. Axelbaum, W.L. Flower, C.K. Law, Dilution and temperature effects of inert addition on soot formation in counterflow diffusion flames, Combust. Sci. Technol. 61 (1–3) (1988) 51–73.
[18] A. Kalbhor, R. Schmitz, A. Ramirez, P. Vlavakis, F.P. Hagen, F. Ferraro, M. Braun-Unkhoff, T. Kathrotia, U. Riedel, D. Trimis, J. Van Oijen, C. Hasse, D. Mira, Experimental and numerical investigation on soot formation and evolution of particle size distribution in laminar counterflow ethylene flames, Combust. Flame 260 (2024) 113220.
[19] A. Brockhinke, M. Letzgus, S. Rinne, K. Kohse-Höinghaus, Energy transfer in the $d^3\Pi_g$–$a^3\Pi_u$ (0–0) swan bands of C_2: Implications for quantitative measurements, J. Phys. Chem. A 110 (9) (2006) 3028–3035.
[20] R. Khare, P. Vlavakis, T.V. Langenthal, A. Loukou, M. Khosravi, U. Kramer, D. Trimis, Experimental investigation of the effect of hydrogen addition on the sooting limit and structure of methane/air laminar counterflow diffusion flames, Fuel 324 (2022) 124506.
[21] C.R. Shaddix, Correcting Thermocouple Measurements for Radiation Loss: a Critical Review, American Society of Mechanical Engineers, New York, NY (US), Sandia National Labs., Livermore, CA (US), 1999.
[22] C. Schulz, B.F. Kock, M. Hofmann, H. Michelsen, S. Will, B. Bougie, R. Suntz, G. Smallwood, Laser-induced incandescence: recent trends and current questions, Appl. Phys. B 83 (3) (2006) 333–354.
[23] H.A. Michelsen, C. Schulz, G.J. Smallwood, S. Will, Laser-induced incandescence: Particulate diagnostics for combustion, atmospheric, and industrial applications, Prog. Energy Combust. Sci. 51 (2015) 2–48.
[24] F.P. Hagen, D. Kretzler, T. Häber, H. Bockhorn, R. Suntz, D. Trimis, Carbon nanostructure and reactivity of soot particles from non-intrusive methods based on UV-VIS spectroscopy and time-resolved laser-induced incandescence, Carbon 182 (2021) 634–654.
[25] F.P. Hagen, R. Suntz, H. Bockhorn, D. Trimis, Dual-pulse laser-induced incandescence to quantify carbon nanostructure and related soot particle properties in transient flows – concept and exploratory study, Combust. Flame 243 (2022) 112020.
[26] F.P. Hagen, D. Kretzler, S. Koch, H. Bockhorn, R. Suntz, D. Trimis, H. Kubach, A. Velji, T. Koch, On-line monitoring of carbon nanostructure and soot reactivity in engine exhaust by dual-pulse laser-induced incandescence, Combust. Flame 254 (2023) 112850.
[27] S. Török, M. Mannazhi, P.-E. Bengtsson, Laser-induced incandescence (2λ and 2C) for estimating absorption efficiency of differently matured soot, Appl. Phys. B 127 (7) (2021) 96.
[28] A. Eremin, E. Gurentsov, R. Kolotushkin, The change of soot refractive index function along the height of premixed ethylene/air flame and its correlation with soot structure, Appl. Phys. B 126 (8) (2020) 125.

[29] T. Lehre, H. Bockhorn, B. Jungfleisch, R. Suntz, Development of a measuring technique for simultaneous in situ detection of nanoscaled particle size distributions and gas temperatures, Chemosphere 51 (10) (2003) 1055–1061.
[30] H.A. Michelsen, F. Liu, B.F. Kock, H. Bladh, A. Boïarciuc, M. Charwath, T. Dreier, R. Hadef, M. Hofmann, J. Reimann, et al., Modeling laser-induced incandescence of soot: a summary and comparison of LII models, Appl. Phys. B 87 (3) (2007) 503–521.
[31] D.R. Snelling, F. Liu, G.J. Smallwood, Ö.L. Gülder, Determination of the soot absorption function and thermal accommodation coefficient using low-fluence LII in a laminar coflow ethylene diffusion flame, Combust. Flame 136 (1) (2004) 180–190.
[32] B. Zhao, Z. Yang, J. Wang, M.V. Johnston, H. Wang, Analysis of soot nanoparticles in a laminar premixed ethylene flame by scanning mobility particle sizer, Aerosol Sci. Technol. 37 (8) (2003) 611–620.
[33] J. Camacho, C. Liu, C. Gu, H. Lin, Z. Huang, Q. Tang, X. You, C. Saggese, Y. Li, H. Jung, L. Deng, I. Wlokas, H. Wang, Mobility size and mass of nascent soot particles in a benchmark premixed ethylene flame, Combust. Flame 162 (10) (2015) 3810–3822.
[34] J.-H. Choi, C.-H. Hwang, S.K. Choi, S.M. Lee, W.J. Lee, S.H. Jang, S.-H. Park, Impacts of hydrogen addition on micro and nanostructure of soot particles formed in C_2H_4/air counter diffusion flames, Int. J. Hydrog. Energy 41 (35) (2016) 15852–15858.
[35] G.P. Smith, D.M. Golden, M. Frenklach, N.W. Moriarty, B. Eiteneer, M. Goldenberg, C.T. Bowman, R.K. Hanson, S. Song, W.C.J. Gardiner, V.V. Lissianski, Z. Qin, GRI-mech 3.0, 1999, http://www.me.berkeley.edu/gri_mech/.
[36] T. Kathrotia, U. Riedel, A. Seipel, K. Moshammer, A. Brockhinke, Experimental and numerical study of chemiluminescent species in low-pressure flames, Appl. Phys. B 107 (3) (2012) 571–584.
[37] P. Sunderland, Effects of structure and hydrodynamics on the sooting behavior of spherical microgravity diffusion flames, Combust. Flame 132 (1–2) (2003) 25–33.
[38] E. Ranzi, A. Frassoldati, A. Stagni, M. Pelucchi, A. Cuoci, T. Faravelli, Reduced kinetic schemes of complex reaction systems: Fossil and biomass-derived transportation fuels, Int. J. Chem. Kinet. 46 (9) (2014) 512–542.
[39] R.L. Axelbaum, C.K. Law, W.L. Flower, Preferential diffusion and concentration modification in sooting counterflow diffusion flames, Proc. Combust. Inst. 22 (1) (1989) 379–386.